Surface Thermal Behavior and RT CO Gas Sensing Application of an Oligoacenaphthylene with *p*-Hydroxyphenylacetic Acid Composite

Praveen Kumar Basivi, Tayssir Hamieh, Kedhareswara Sairam Pasupuleti, Visweswara Rao Pasupuleti, Vempuluru Navakoteswara Rao, Moon-Deock Kim, and Chang Woo Kim*

Read Online
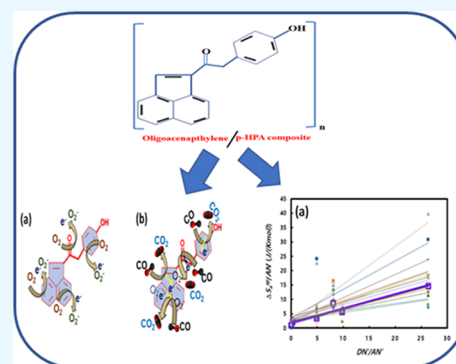
ACCESS | Metrics & More | Article Recommendations | Supporting Information

ABSTRACT: The current work describes room-temperature gas sensing performances using an oligoacenaphthylene (OAN)/*p*-hydroxyphenylacetic acid (*p*-HPA) composite. Based on inverse gas chromatography (IGC), the London dispersive surface energy γ_s^d is calculated by using 14 representative models. Even when the γ_s^d values of both OAN and the OAN/*p*-HPA composite are decreased as the temperature increases, the surface of OAN shows a higher value than that of the composite. The Gibbs surface free energy values of both are decreased with an increasing temperature. In our results, higher Lewis basic characters are observed in OAN and the OAN/*p*-HPA composite and the OAN/*p*-HPA surface exhibits a higher basicity compared to OAN. Because of the presence of phenolic groups in the OAN/*p*-HPA composite, the more important basic character drives a significant CO gas sensing ability with a sensitivity of 8.96% and good cycling stability as compared to the pristine counterparts. It is expected that the current study sheds light on a new pathway to exploring polymer composite materials for futuristic diverse and multiple applications, including IGC and gas sensor applications.

1. INTRODUCTION

The surface energetics of pharmaceutical solids usually impact their interaction with another liquid or solid under close association. The interfacial energy is refined at the interface when two such condensed systems interact. The magnitude of this interfacial energy depends on the individual surface energies of the two systems. The interfacial energy consequences depend on several factors such as binding of a film to a tablet, wetting, wet granulation, spreading of a liquid over a solid surface, dissolution and the suspension formulation of a drug. Specific techniques are possible for measuring the surface energetics of a solid; however, inverse gas chromatography (IGC) has been verified to be an impressive and facile technique.[1−5]

For decades, conducting polymer derivatives have received special attention due to their potential applications in various fields, including sensors, electrochromic display devices, energy storage systems, biosensors and antistatic coatings. Oligoacenaphthylene (OAN) is used in electrodeposition by direct anodic oxidation of an acenaphthylene boron trifluoride diethyl etherate medium. OAN is known as a light-harvesting or antenna polymer containing an acenaphthylene chromophore. It can be described as an appreciable rigid polymer exhibiting a non-draining character. OAN exhibits good stiffness as indicated by examination of molecular models.[6−9]

On the other hand, *p*-hydroxyphenylacetic acid (*p*-HPA) has been widely used for the treatment of pulmonary hepatitis B

and carcinoma diseases. *p*-HPA is an active component of the herb *Aster tataricus*. Most reports indicated that *p*-HPA is a metabolite of aromatic amino acid catabolism that is secreted in saliva, controls NadA gene expression and response to cold, and finally becomes a potential hypo-pigmenting agent. *p*-HPA could inhibit hypoxia-inducible factor 1-alpha (HIF-1α) expression, and is also mainly used in seawater aspiration-induced lung injury.[10,11]

The surface energy parameters of pure OAN have been compared with the parameters obtained for *p*-HPA blends. The effect of OAN on the surface energy of *p*-HPA has been evaluated. The dispersive surface free energy component is the most important physical parameter.[12−15] The London dispersive surface free energy component γ_s^d (T) as a function of temperature has been assessed by using nine different models all based on the Fowkes relation. Two models, the Dorris−Gray relation[16] and Hamieh−Dorris−Gray model[17] and six models, the Kiselev, cylindrical, geometric, spherical, van der Waals and Redlich−Kwong−Hamieh models have been applied using six molecular methods for determining the
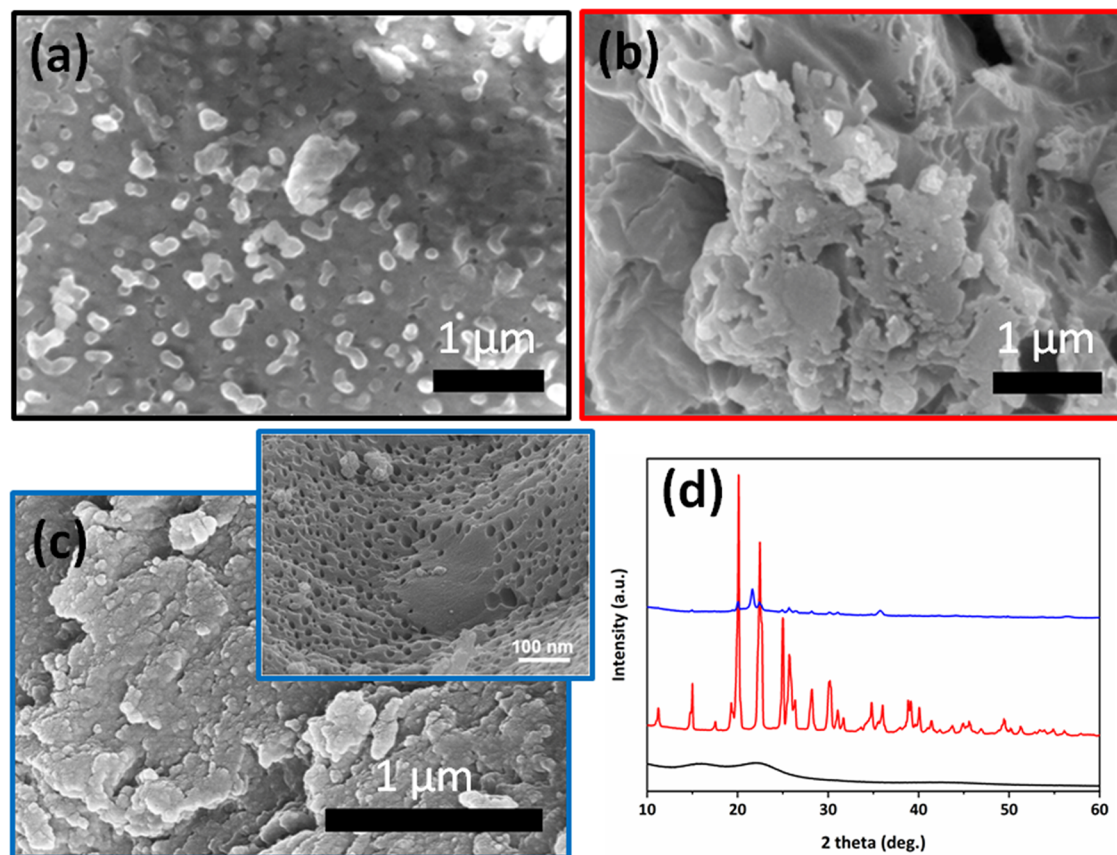
Figure 1. SEM images of (a) pristine OAN (b) pristine *p*-HPA and (c) the OAN/*p*-HPA composite with an inset image (low magnification indicating the porous nature); (d) XRD patterns of OAN (black), *p*-HPA (red) and the OAN/*p*-HPA composite (blue).

surface areas of organic molecules.[18] The Gibbs specific component of the surface free energy ΔG_a^{sp} was also determined by using the above molecular models and IGC methods such as the Dong, Sawyer and Brookman,[19] Saint Flour–Papirer,[20] Donnet et al.,[21] Brendlé–Papirer,[22] Hamieh,[23] enthalpy of vaporization[23,24] and enthalpy of formation[23] methods were used to evaluate the Gutmann Lewis acid–base parameters.

In recent years, room-temperature (RT) gas sensing applications using polymers and their composite derivates have attracted great research attention in human health, environmental monitoring, etc., owing to their wide material variety, flexibility, good electrical mobility, light weight, compatibility and large-scale manufacturing methods.[25−27] In particular, carbon monoxide (CO) has become one of the most toxic and dangerous pollutant gases that are generated from the combustion process of automobiles and power stations, etc., which causes severe health hazards.[27,28] A few parts per million of inhaled CO gas can easily react with hemoglobin and produce carboxyhemoglobin, which further affects the oxygen supply to the body tissues, causing dizziness, nausea and difficulty in breathing.[28,29] The characteristics of CO gas such as being odorless, colorless and tasteless, have required development of a highly sensitive sensor using polymer composites with high selectivity, reproducibility and sensitive detection at RT.[27,29,30]

Herein, we demonstrate the surface thermodynamic characteristics of OAN, *p*-HPA and OAN/*p*-HPA composites by IGC. Three polymeric samples are characterized for RT CO gas detection in terms of surface area, porosity, and functional groups. The gas sensing properties of polymer composites are mainly affected by their surface morphology, surface-to-volume ratio, porosity and functional groups.[30,31] The synergetic combination of OAN and *p*-HPA composites can produce strong interfacial bonding between polymeric chains that further actively participate in the CO gas adsorption, leading to a change in electrical resistance.[27] To the best of our knowledge, the current work is the first report that discusses the surface thermodynamic characteristics using IGC and practical RT CO gas sensing application using OAN, *p*-HPA and OAN/*p*-HPA composites.

2. METHODS

2.1. Models. The fundamental parameter of IGC is the net retention volume V_n of organic molecules adsorbed on solid surfaces. This parameter is obtained from the net retention time. By using the Kemball and Rideal reference state[32] given at $T_0 = 0°C$ by $P_0 = 1.013 \times 10^5$ Pa and $\pi_0 = 6.08 \times 10^{-5}$ N m^{-1} it is possible to determine the standard free energy ΔG_a^0 of adsorption of the adsorbed organic molecules (eq 1):

$$\Delta G_a^0 = -RT \ln V_n + RT \ln\left(\frac{P_0}{sm\pi_0}\right) \tag{1}$$

where R is the ideal gas constant, T is the absolute temperature, m is the mass of the solid, and s is its specific surface area.

The free energy of adsorption ΔG_a^0 of any molecules on a solid substrate is equal to the sum of the dispersive ΔG_a^d and specific ΔG_a^{sp} contributions as follows:
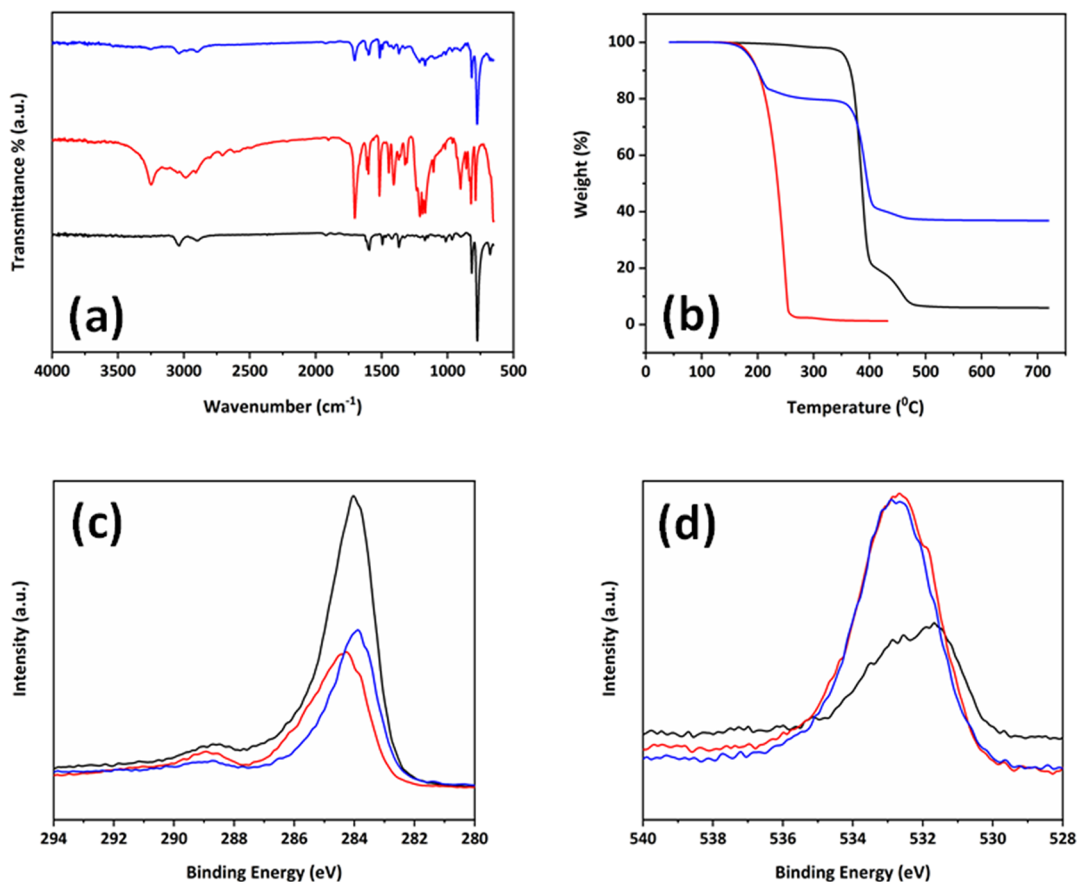
Figure 2. (a) FTIR, (b) TGA, and (c) C 1s and (d) O 1s XPS core-level spectra of OAN (black), *p*-HPA (red) and the OAN/*p*-HPA composite (blue).

$$\Delta G_a^0 = \Delta G_a^d + \Delta G_a^{sp} \tag{2}$$

The specific contributions of the free energy of adsorption of the probes can be determined by using one of the following thermodynamic characteristics: the boiling point (BP),[19] the vapor pressure P_0,[20] the deformation polarizability α_0,[21] the topological index χ_T,[22] the standard enthalpy of vaporization ΔH_{vap}^0,[24] the enthalpy of vaporization as a function of temperature $\Delta H_{vap}^0(T)$,[23] and the standard enthalpy of formation ΔH_f^{0}[23] of the injected solvents. ΔG_a^{sp} can be also obtained by using the Fowkes relation based on the values of the surface area of molecules. The Hamieh model[23] considering the thermal effect and six molecular methods, called Kiselev, cylindrical, van der Waals, Redlich–Kwong, spherical and geometric models gave the surface areas of organic molecules.

The above methods and models were used to determine the dispersive (London) and polar (specific) components of the free energy of adsorption. By determining the specific free energy of adsorption ΔG_a^{sp} of organic molecules against the temperature, we were able to deduce the specific enthalpy ΔH_a^{sp} and entropy ΔS_a^{sp} of polar solvents adsorbed on the solid surfaces, by using eq 3:

$$\Delta G_a^{sp} = \Delta H_a^{sp} - T\Delta S_a^{sp} \tag{3}$$

Knowing ΔH_a^{sp} and the normalized donor DN′ and acceptor AN′ numbers of electrons of the various probes,[33−36] one obtained the acid K_A and base K_D constants of the solid surfaces from eq 4.[37−40]

$$(-\Delta H_a^{sp}) = K_A DN' + K_D AN' \tag{4}$$

Furthermore, the dispersive component of the surface tension of the probe γ_l^d and the surface area of molecules allowed calculating the surface energy of the solid by using the Fowkes relation.[38]

$$-\Delta G_a^0 = 2Na(\gamma_l^d \gamma_s^d)^{1/2} + (-\Delta G_a^{sp}) \tag{5}$$

where N is Avogadro's number and a is the surface area of one adsorbed molecule on the solid.[36−38] γ_s^d was also determined by using the Dorris and Gray relation[16] and Hamieh model.[41−43]

2.2. Composite Preparation. One gram (wt %) of OAN, 1 g (wt %) of *p*-HPA and 1 g (wt %) of Chromosorb (80–120) mesh were taken into a round-bottom flask and dissolved in 100 mL (v/v) of ethanol and methanol. The reaction mixture was thoroughly stirred for 12 h, with an 800 rpm speed at 25 °C with a magnetic stirrer bar. The solvent was allowed to evaporate by using a rotavapor and a vacuum oven at 50 °C for 12 h and then dried and collected. The ratio was taken in order to bind the materials accurately without changing the properties. As an inert material, Chromosorb is a binding material that does not modify the sample properties. The Chromosorb surface area[44] is 0.5 m²/g in the schematic diagram in Figure S1.

3. RESULTS AND DISCUSSION

3.1. Morphology and Structures. Figure 1 displays typical SEM images of the as-prepared materials OAN, *p*-HPA

and blend of OAN with *p*-HPA (OAN/*p*-HPA). The SEM micrograph of OAN shows an ordered arrangement of polymeric chains with a granular-like morphology in Figure 1a.[45] The SEM image of *p*-HPA displays a thick lamellar-like layered structure in Figure 1b. Figure 1b shows an ordered arrangement of polymeric chains with some agglomerate formation. After the blending of OAN into *p*-HPA the morphology of the composite material was changed as shown in Figure 1c,[25,27] in which the micrograph of the composite material shows a two-phase morphology with an aggregated lamellar structure containing a small particle. The SEM image of OAN/*p*-HPA shows a porous nature with structural segregation caused by the modification inside the polymer matrix in the formation of a chemical blend between the OAN and *p*-HPA materials. The zoomed view of the OAN/*p*-HPA composite material indicates that the as-prepared material has a porous nature as shown in the inset image of Figure 1c. The SEM images of the as-prepared samples show the semi-crystalline nature of OAN and the OAN with *p*-HPA blend. The crystalline properties of the OAN and OAN with *p*-HPA blend samples were analyzed with XRD as shown in Figure 1d. The XRD results indicate that OAN has a purely amorphous structure and *p*-HPA has a more highly crystalline structure. The OAN/*p*-HPA blended sample exhibits a semi-crystalline nature as observed from a decrease in peak intensity. This shows that *p*-HPA was successfully incorporated into the polymeric matrix of OAN. This causes a structural defect inside the composite material that provides an active site for the effective absorption of gas molecules.

3.2. Surface Characteristics. The structural and functional groups of the as-prepared OAN, *p*-HPA and OAN/*p*-HPA blend were characterized using FTIR analysis as shown in Figure 2a. OAN exhibits bands at around 3050 and 500 cm^{-1} corresponding to the characteristic bands of sp^2 C−H and sp^2 C−C stretching. The band at around 1700 cm^{-1} corresponds to C=O stretching in aromatic carbonyl groups. The band present at 565 cm^{-1} corresponds to C=N stretching, suggesting the characteristic peak of OAN.[46,47] *p*-HPA exhibits strong bands at around 3300 and 1200 cm^{-1} corresponding to O−H and C−O stretching in aromatic hydroxy and carboxylic acids. The intense peak located at 1272 cm^{-1} is ascribed to the amine functional groups of −NH$_2$ and =O−NH$_2$ termination bonds.[48] However, the composite material composed of OAN and *p*-HPA exhibits almost all of the characteristic bands of both individuals, which are located in the range of 3300 to 1200 cm^{-1}. The band at 1700 cm^{-1} is ascribed to C=O, and the peak at 3300 cm^{-1} with a low intensity (diminished) suggests the successful formation of the hybrid composite. The spectrum of the composite material shows peak wagging and the absence of bands as compared to the individual spectra. This indicates clearly that hybridization exists in the OAN and *p*-HPA composite material. A large number of surface-active sites help enhance the gas molecule adsorption.

Because the test for thermal stability is related to significantly dynamic ways of detecting the degradation behavior OAN, *p*-HPA and the OAN/*p*-HPA composite were monitored by TGA as shown in Figure 2b. OAN has three phases of decomposition. In the initial phase, it is stable up to 350 °C with 4% decomposition. Upon increasing the temperature to 400 °C, it is decomposed rapidly to 79% and finally shows a decomposition of 93% at 474 °C. *p*-HPA showing two phases of decomposition, shows only 1%

decomposition up to 154 °C and is decomposed by 97% at 243 °C. The OAN/*p*-HPA composite, showing five phases of decomposition is initially stable up to 150 °C with 1% weight loss and the weight loss increases to 17% at 215 °C. The weight loss corresponds to 22% at 350 °C and 60 and 63% at 410 and 470 °C, respectively. The TGA analysis clearly suggests that the composite material is thermally stable at about 150 °C and a proper candidate for CO gas sensing application.

XPS was employed to study the surface chemistry of OAN, *p*-HPA and the OAN/*p*-HPA composite. The carbon (C 1s) peaks of OAN, *p*-HPA and the OAN/*p*-HPA composite blend appear at 284.06, 283.9 and 284.53 eV respectively, in Figure 2c. It is observed that binding energy shifting to 284.53 eV appear toward the composite. The O 1s peaks of OAN, *p*-HPA and the composite are shown at 531.7, 532.7 and 533.2 eV respectively. The peak shifting in the C 1s and O 1s spectra of the OAN/*p*-HPA composite indicates clear evidence of the charge transfer between OAN and *p*-HPA with the chemical functional groups in the polymer matrix. The increase in binding energy in the composite indicates that *p*-HPA was successfully incorporated into the OAN composite.[27,48,49] The deconvoluted C 1s spectra of the OAN/*p*-HPA composite show three typical peaks located at 283.88, 284.48 and 288.88 eV corresponding to C−C, C−O and C=O[27,50] in Figure S2 (Supporting Information). The O 1s spectra of the OAN/*p*-HPA composite was resolved into two peaks positioned at 532.78 and 534.78 eV which were attributed to C=O and C−OH bonds.[27] The charge transfer between the polymer matrix and the evolved functional groups of the OAN/*p*-HPA composite provides active surface sites, which further help improve the gas molecule absorption.[27,50]

3.3. IGC Study. *3.3.1. Variations of the RT ln $V_n(T)$ Gibbs Free Energy of Adsorption.* The RT ln V_n values of *n*-alkanes and polar probes were measured by IGC for the OAN and OAN/*p*-HPA composite columns at five temperatures from 343.15 to 383.15 K. In Table S1 (Supporting Information), the obtained RT ln V_n values of OAN and the OAN/*p*-HPA composite are shown. The RT ln V_n values in the two cases of OAN and the OAN/*p*-HPA composite showed a decrease when the temperature increased because of the increasing desorption rate. The RT ln V_n values in Table S2 allowed deducing the values of the free energy of adsorption ΔG_a^0 of all solvents adsorbed on the solid surfaces (Table S2) by using eq 1. The variations of RT ln $V_n(T)$ (Figure S3) and $\Delta G_a^0(T)$ (Figure S4) as a function of temperature were found to be linear for *n*-alkanes and polar molecules adsorbed on the OAN and OAN/*p*-HPA surfaces. The negative values of $\Delta G_a^0(T)$ obtained for all used solvents revealed the spontaneous process of adsorption of solvents on solid surfaces.

The dispersive component of surface energy γ_s^d (mJ/m^2) of OAN and the OAN/*p*-HPA composite as a function of temperature was calculated by using nine molecular models including the Dorris−Gray and Hamieh thermal models in Table S3. The obtained results are plotted as line graphs in Figure S5. The values of γ_s^d of OAN were proved to be higher than those of the OAN/*p*-HPA composite for all temperatures in Figure 3. Table S4 shows that ratios of the $\gamma_s^d(T)$ of OAN and OAN/*p*-HPA are greater than 1 for various molecular models of *n*-alkanes at various temperatures. Table S4 proves the following equation:

$$1 < \gamma_s^d(\text{OAN})/\gamma_s^d(\text{OAN}/p-\text{HPA}) < 1.7 \qquad (6)$$
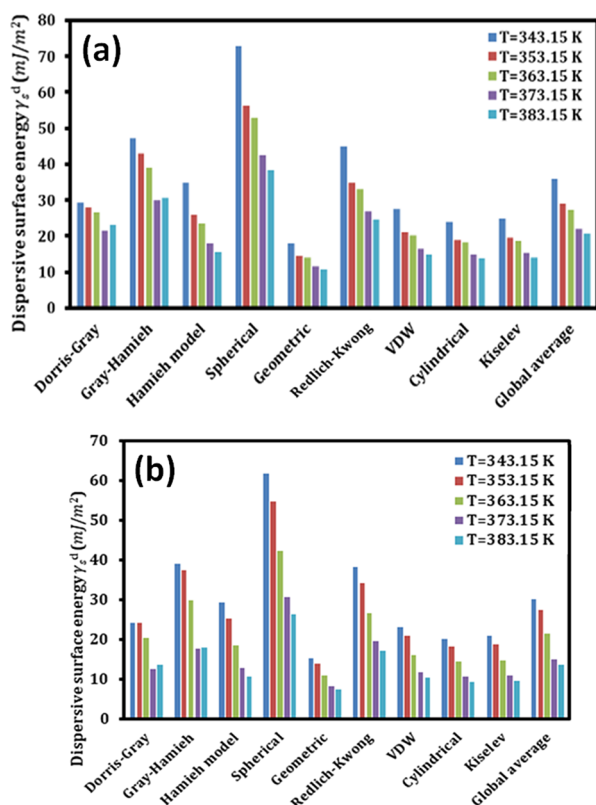
Figure 3. Dispersive surface energies γ_s^d (mJ/m^2) of (a) OAN and (b) OAN/p-HPA following the various methods and models for five temperatures.

The dispersive surface energy $\gamma_s^d(T)$ of pure OAN shows larger values than those of the OAN/p-HPA composite due to the addition of p-HPA to OAN. In terms of chemical and/or physical polymer interactions, the functional groups present in p-HPA, i.e., R−C≡O−OH and C$_6$H$_5$−OH, interact with OAN active surface sites. Physical interactions appear in the blending of the OAN/p-HPA composite. This leads to a decrease in the London dispersive surface free energy of OAN/p-HPA and therefore to a larger value of the γ_s^d of OAN.[17] The ratio $\gamma_s^d(\text{OAN})/\gamma_s^d(\text{OAN}/p-\text{HPA})$ increases when the temperature increases showing that temperature is a more important factor on the London dispersive surface free energy of OAN/p-HPA.

Our calculation also revealed that variations of the $\gamma_s^d(T)$ of OAN and the OAN/p-HPA composite are linear, indicating a good regression coefficient. A decrease in $\gamma_s^d(T)$ versus temperature was observed for the various molecular models. In Table S5, the different equations for $\gamma_s^d(T)$, the dispersive surface entropy ε_s^d, the extrapolated values of $\gamma_s^d(T = 0 \text{ K})$ and the regression coefficient R^2 were obtained by using the different molecular models. More precise values of $\gamma_s^d(T)$ were obtained by the Hamieh model considering the thermal effect on the surface area of organic solvents. The following are relations for the $\gamma_s^d(T)$ of OAN and the OAN/p-HPA composite using the Hamieh model:

$$\gamma_s^d(T)\ (\text{OAN}) = -0.46T + 191.48 \tag{7}$$

$$\gamma_s^d(T)\ (\text{OAN}/p-\text{HPA}) = -0.50T + 200.43 \tag{8}$$

3.3.2. Specific and Lewis Acid−Base Properties. By applying the various IGC methods and models, we obtained

the values of the specific Gibbs free energy $(-\Delta G_a^{sp})$ of the adsorption of organic solvents on the various polymeric materials by using the values in Table S2 and applying eqs 2 and 5. Tables S6 and S7 show the obtained values of the $(-\Delta G_a^{sp})$ of different polar solvents adsorbed on OAN and the OAN/p-HPA composite as a function of temperature by using the different molecular models and IGC methods. The $(-\Delta G_a^{sp})$ of all adsorbed organic solvents for the two solid substrates decreases with the temperature increases for all IGC methods and models. The specific Gibbs free energy of an adsorbed solvent on one solid surface can vary from one to two times that of the second material.

In the OAN polymer, the lowest $(-\Delta G_a^{sp})$ value was observed for the DEE and THF solvents for the 14 methods, whereas the highest $(-\Delta G_a^{sp})$ value was obtained for the DCM, TCM, EA and AC solvents for the different methods. The strong interaction obtained with the Lewis acidic solvents suggested that the OAN polymer exhibited a basic rather than an acidic character. The lowest $(-\Delta G_a^{sp})$ value of the OAN/p-HPA composite was observed with the DEE, THF and EA solvents for all methods and molecular models. The highest values of $(-\Delta G_a^{sp})$ were obtained when using acidic solvents, also suggesting the basic character of the OAN/p-HPA composite. The IGC results obtained with two solid surfaces thus proved their Lewis amphoteric properties with an important basic tendency for the two polymers.

The linear variations of $(-\Delta G_a^{sp})\ (T)$ against the temperature (Figure S6) relative to the adsorption of polar molecules on OAN (Figure S3) and the OAN/p-HPA composite (Figure S7) allowed the determination of the specific enthalpy of adsorption $(-\Delta H_a^{sp})$ and specific entropy of adsorption $(-\Delta S_a^{sp})$ of the different polar probes by using a classical thermodynamic relation. The curves of Figures 4 and 5 prove that we obtained linear variations of $(-\Delta G_a^{sp})\ (T)$ with a good linear regression coefficient approaching unity for OAN and OAN/p-HPA surfaces and for all of the used IGC methods and models.

In Tables S8 and S9, the values of the $(-\Delta H_a^{sp})$ and $(-\Delta S_a^{sp})$ of the various polar solvents adsorbed on OAN and OAN/p-HPA surfaces by using the various molecular models, Hamieh model, topological index, deformation polarizability, vapor pressure, BP, standard enthalpy of vaporization and enthalpy of formation methods compared to the global average. Furthermore, the ΔH_a^S values along with Gutmann Lewis acid−base parameters are used in eq 9 to evaluate the Lewis acid−base parameters. Equation 4 was applied by using the normalized acceptor AN′ and donor DN′ numbers of the polar solvents[34,36,39] and the values from Tables S8 and S9 to draw in Figures 4 and 5 respectively. The variations of $(-\Delta H_a^{sp})/\text{AN}′$ and $(-\Delta S_a^{sp})/\text{AN}′$ as a function of the DN′/AN′ of the different polar molecules adsorbed on OAN and OAN/p-HPA surfaces. This allowed evaluating the enthalpic and entropic Lewis acid−base parameters of the solid substrates, of acidic K_A and basic K_D constants.

One obtained the values of the enthalpic acidic K_A and basic K_D constants of the two studied polymers from the slope and intercept of the liner plots respectively, for all 14 methods and models whereas the entropic acidic ω_A and basic ω_D constants were obtained from the following equation:

$$(-\Delta S_a^{sp}) = \omega_A \text{DN}′ + \omega_D \text{AN}′ \tag{9}$$

In Table S8, shown are the calculated values of the enthalpic and entropic acid−base constants of the two solid materials as
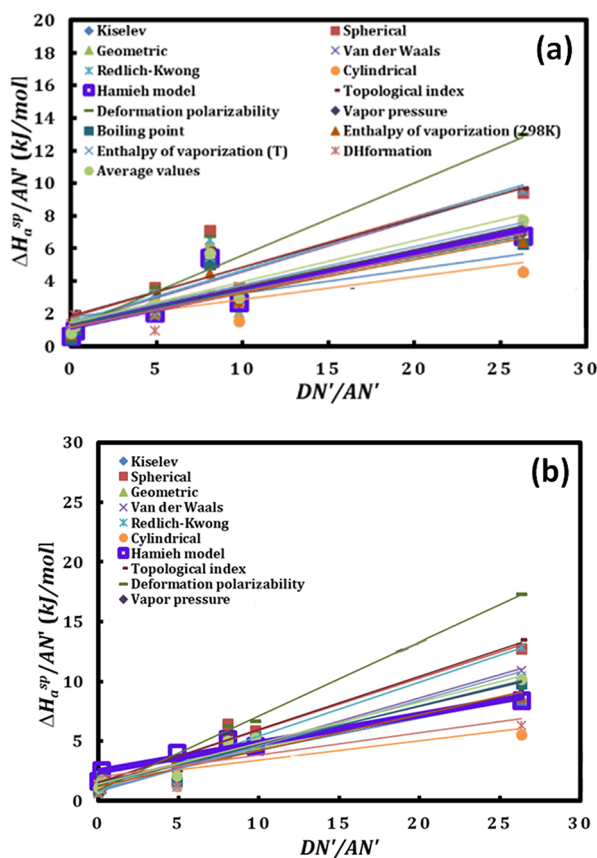
Figure 4. Variations of $\left(\frac{-\Delta H_{a}^{sp}}{AN'}\right)$ as a function of the $\left(\frac{DN'}{AN'}\right)$ of different polar molecules adsorbed on (a) OAN and (b) OAN/p-HPA surfaces for different molecular models and IGC methods.

Figure 5. Variations of $\left(\frac{-\Delta S_{a}^{sp}}{AN'}\right)$ as a function of the $\left(\frac{DN'}{AN'}\right)$ of different polar molecules adsorbed on (a) OAN and (b) OAN/p-HPA surfaces for different molecular models and IGC methods.

well as their acid base ratios by using the above 14 molecular models and IGC methods. We observed that the linearity in the two previous cases of the acid−base constants are satisfied but in some models the regression coefficients are relatively good. The best linear relation was obtained by the Hamieh model based on the thermal effect on the surface area of organic molecules.

The values of K_A, K_D, ω_A and ω_D Lewis acid base parameters of the OAN and OAN/p-HPA polymers are given in Table S10. It is shown that the OAN/p-HPA composite exhibits a stronger acid−base character than the OAN surface. The obtained values of the different acid base parameters of the two surfaces from Hamieh model are as follows:
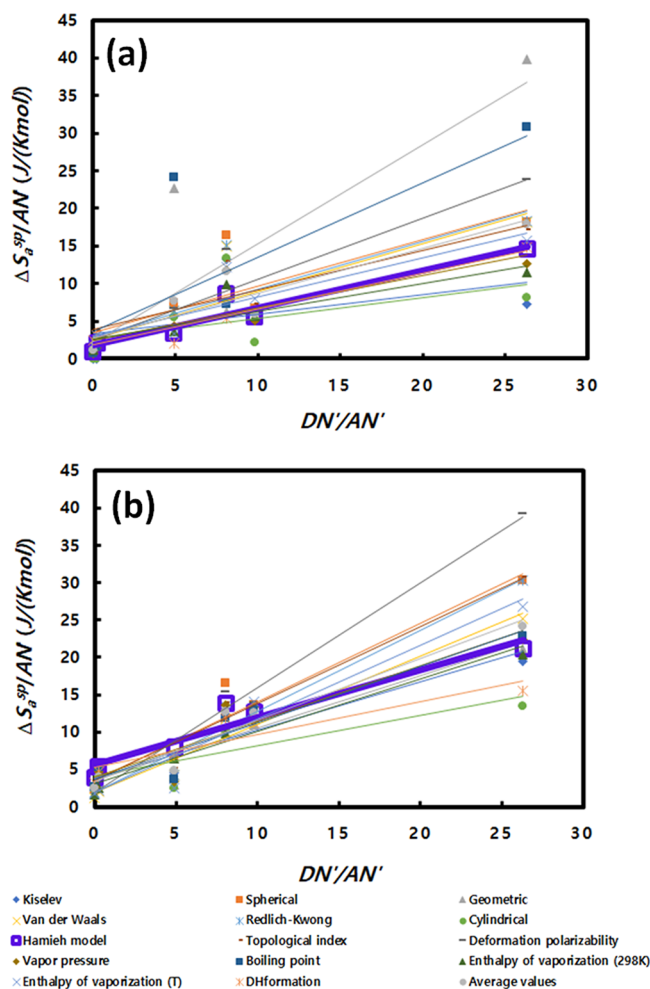
For OAN:

$$K_A = 0.134, K_D = 0.733, K_D/K_A = 5.453; \omega_A$$
$$= 0.30 \times 10^{-3} \text{ and } \omega_D = 1.1 \times 10^{-3}, \omega_A/\omega_D = 3.5 \tag{10}$$

For the OAN/p-HPA composite:

$$K_A = 0.141, K_D = 1.482, K_D/K_A = 10.518; \omega_A$$
$$= 0.38 \times 10^{-3} \text{ and } \omega_D = 3.4 \times 10^{-3}, \omega_D/\omega_A = 8.9 \tag{11}$$

The results clearly showed that the two materials are amphoteric with an accentuated basic character and the OAN/p-HPA composite is more basic than OAN.

The K_A and K_D values are related to the amount of the acidic and basic sites on the surface; we deduced that both surfaces contain more basic sites and a smaller number of acidic sites owing to the presence of basic phenol groups in the OAN/p-HPA surface. Furthermore, the basic sites are higher in the OAN/p-HPA composite than in OAN. This resulted from the presence of strong R−C≡O−OH and C_6H_5−OH groups in the p-HPA molecule. Therefore, based on the above results, it may be concluded that the addition of p-HPA to OAN causes an increase in basic parameters while the acidic parameters almost remain constant.

3.4. CO Gas Sensing. The three kinds of composites, OAN, p-HPA and OAN/p-HPA, were tested for practical CO gas sensing at RT as shown in Figure 6. Figure 6a displays the time-dependent sensitivity plots of OAN, p-HPA and OAN/p-HPA composite sensors under exposure to 100 ppm CO gas at RT. The bare p-HPA sensor shows a negligible response to 100 ppm CO gas. The bare OAN sensor exhibits a sensitivity of about 3.62% to CO gas, whereas the OAN/p-HPA composite sensor shows an impressive gas sensing response to CO gas with a sensitivity of about 8.96%, which is nearly 2.5 times and 8.5 times higher than those of the pristine parts. The OAN/p-HPA composite sensor was tested under various concentrations from 5 to 100 ppm CO gas at RT as shown in Figure
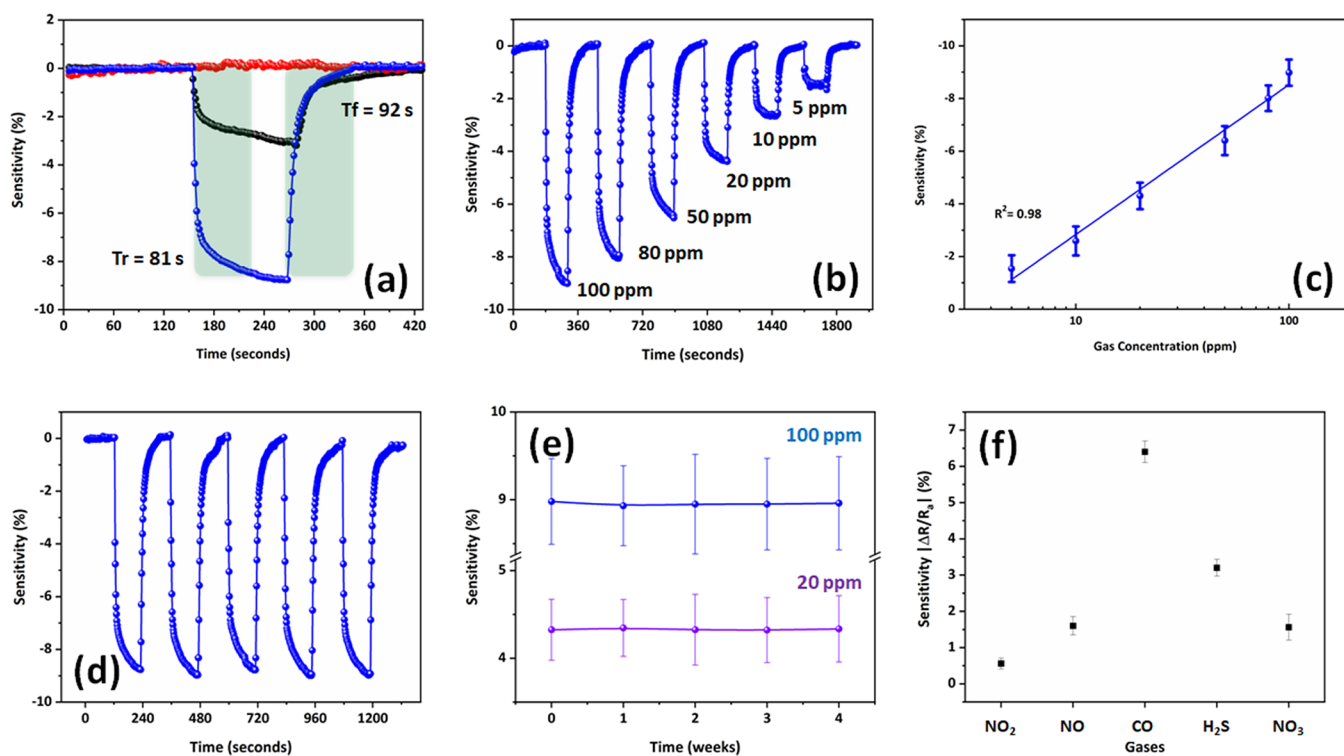
Figure 6. (a) Dynamic gas sensing properties of OAN, p-HPA and OAN/p-HPA composite under CO of 100 ppm at RT, (b) RT CO gas sensing response curves of OAN/p-HPA composite under various gas concentrations, (c) summary of the sensitivity of OAN/p-HPA composite plotted between gas concentration versus sensitivity, (d) cycling stability, (e) long term reproducibility and (f) selectivity test of OAN/p-HPA composite.

Table 1. Comparison of the CO Gas Sensing Performances of the OAN/p-HPA Composite Material with Previous Reports

S no	sensing materials	CO gas (ppm) @ operating temperature (°C)	sensitivity (R_a/R_g or $R_a - R_g/R_a \times 100$)/ppm	response/recovery time (s)	ref
1	$ZnO/La_{0.8}Sr_{0.2}Co_{0.5}Ni_{0.5}O_3$	100 @ 200	16.4	~16/43	53
2	Pd-decorated TiO nanotube	100 @ 200	1.25	~21/39	54
3	CuO with Pd nanoparticles	100 @350	1.15	~298/265	55
4	Pani−MWCNT	500 @ RT	6.8	76/210	56
5	Au−CoOOH	100 @ 80	5.1	60/65	57
6	Ppy−FeTPPCI	300 @ RT	12	500/200	58
7	graphene oxide on PET substrate	100 @ RT	5.6	40/70	59
8	Ppy−PEDOT: PSS	100 @RT	9.8	130/221	27
9	Pani/zeolite	100 @ 100	7.1		60
10	oligoacenaphthylene/p-HPA composites	100 @ RT	8.96	81/92	our work

6b. The composite sensor exhibited a step-growth increment in sensitivity (negatively), which increased as CO gas concentrations increased. However, the original baseline sensitivity value (resistance, not shown here) was achieved when CO gas molecules were turned off and dry air was introduced into the test chamber. The observed changes in the sensitivity with respect to the CO gas concentration were due to the physical adsorption on the active composite sensing layer. Moreover, the high sensitivity was ascribed to the synergetic effect of the blending of OAN/p-HPA composite materials. A linear nature in composite sensor shows that the sensitivity of sensor was enhanced with an increasing CO gas concentration as shown in in Figure 6c. The linearity of R^2 = 0.985 clearly indicates that polymeric composite sensor has a more reliable and stable CO gas sensing performance.[27,47] The repeatability and cycling stability of OAN/p-HPA sensor were tested under 100 ppm CO gas at RT as shown in Figure 6d. The composite sensor exhibited a stable sensitivity response to CO gas for five

repeatable cycles without any loss in sensor sensitivity. The long-term reproducibility was studied under the two different concentrations of 20 and 100 ppm CO gas for up to 4 consecutive weeks as shown in Figure 6e. The long-term stability toward 100 ppm CO gas of the as-prepared composite sample is presented in Figure S8. The polymeric composite sensor shows impressive stability toward CO gas without any degradation in sensitivity. This implies that the composite sensor has good reproducibility. Apart from sensitivity, reproducibility, and cycling stability, selectivity is the foremost factor for a practical sensing application. The selectivity of the composite sensor was tested with different gas analytes such as CO at 50 ppm and NO, NO_2, H_2S and NH_3 at 100 ppm at RT. The results clearly signify that the composite sensor has an excellent sensitivity to CO gas among the other target gases as shown in Figure 6f. Based on various sensing materials such as polymers, metal oxides, and some heterostructures, the CO gas sensing performances of the polymeric composite sensor are
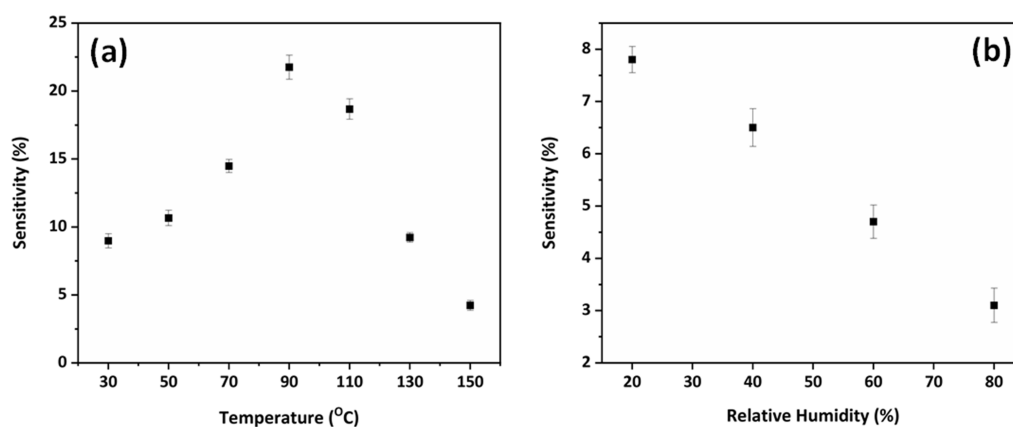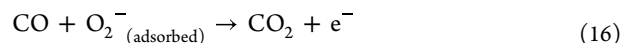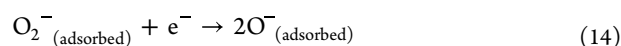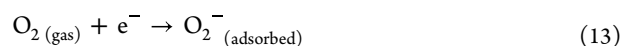
Figure 7. (a) Dynamic gas sensing at different temperatures and (b) relative humidity test of the OAN/*p*-HPA composite under 100 ppm CO at RT.

summarized with previously published reports in Table 1. Compared to the reported gas sensors, the polymeric composite sensor showed enhanced gas sensing performances under CO at RT suggesting a great boom in sensing applications.

The temperature dependence of the dynamic CO gas sensing of the polymeric composite sensor was tested under varying operating temperatures of RT and 50, 70, 90, 110, 130 and to 150 °C as shown in Figure 7a. The OAN/*p*-HPA composite sensor showed a maximum sensitivity of about ~22.7% to CO gas at 90 °C. The sensitivity of the sensor diminished as the temperature rose due to the phase transition temperature of about 151 °C estimated from TGA curves.[27] As the operating temperature reached the Curie temperature, the bonds inside the polymeric sensor became weak to react with the target gas molecules at the Curie temperature and resulted in decreasing sensitivity. The composite sensor was tested on operating humidity for the practical gas sensing application in an RT environment. In order to evaluate the influence of humidity on RT CO gas sensing, the sensitivity of the composite sensor was tested at different relative humidity (RH) values of 20, 40, 60 and 80% as shown in Figure 7b. Note that the composite sensor sensitivity decreased as the RH values increased because active surface sites were blocked by water molecules at higher RH conditions. This resulted in hindering the gas sensing reactivity between the target gas and the sensing material surface layer.[27]

3.5. Mechanism. The mechanism on the CO gas sensing performance of the OAN/*p*-HPA composite is illustrated in Figure 8. A typical chemiresistive gas sensor mainly relies on the change in the electrical resistance of the sample material.[27,46,51] The OAN/*p*-HPA composite showed an n-type semiconducting behavior based on its HOMO−LUMO levels.[45] In Figure 8a, the oxygen molecules are physiosorbed

on the OAN/*p*-HPA composite surface and capture the electrons from the material surface to form adsorbed oxygen ions such as O_2^- and O^- under ambient air. This leads to the formation of an electron depletion layer as shown in eqs 12−15.[27,29,52]

$$O_{2\,(gas)} \rightarrow O_{2\,(adsorbed)} \tag{12}$$

$$O_{2\,(gas)} + e^- \rightarrow O_2{}^-_{(adsorbed)} \tag{13}$$

$$O_2{}^-_{(adsorbed)} + e^- \rightarrow 2O^-_{(adsorbed)} \tag{14}$$

$$O^-_{(adsorbed)} + e^- \rightarrow O^{2-}_{(adsorbed)} \tag{15}$$

$$CO + O_2{}^-_{(adsorbed)} \rightarrow CO_2 + e^- \tag{16}$$

Meanwhile, the OAN/*p*-HPA composite sample was tested under ambient CO gas as shown in Figure 8b. The adsorbed CO gas molecules react with the ionosorbed oxygen species and penetrate into the porous composite sample. They form a strong chemical bond with the blended polymer chains, leading to enhancement of the CO gas sensing reactivity.[27,52] The polar nature of the OAN/*p*-HPA composite helps make the bond between the polar components stronger. As a reducing agent, the CO gas with a lone pair of electrons attaches easily to the OH, C−H, C═O, amine and polar groups of the composite material and facilitates the enhancement of the gas molecule adsorption, diffusion and reactivity. In particular, the adsorbed CO gas molecules form a chemical bond with the carbonyl functional groups in the active sensing material. Based on eq 16, it donates electrons to the conduction band of the n-type OAN/*p*-HPA composite through the charge-transfer process between the composite layer and gas analytes. As such, a greater value of the charge carrier density causes a decrease in the width of the depletion layer and results in an increase in electrical conductivity.[27,51,52] Note that the gas sensing responses and sensitivity depend on the gas adsorption kinetics over the sensing layer. CO gas molecules are physically adsorbed on the material surface at RT and their chemical bond further results in the sensitivity of the sensor. At high-temperature conditions, CO gas molecules are chemically adsorbed on the surface material. This indicates that faster gas molecule adsorption kinetics results in a high gas sensing response with good sensitivity. Thus, higher sensitivity was obtained at a higher temperature compared to that at RT for the polymeric composite sensor. The functional groups, active
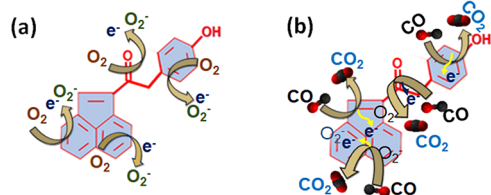
Figure 8. Suggested gas sensing mechanism of the OAN/*p*-HPA composite under (a) ambient air and (b) ambient CO gas at RT.

surface sites and porous morphology of the polymeric composite provides active trap sites for the higher absorption of CO gas molecules. This results in enhanced sensitivity as compared to those of the pristine counterparts.

4. CONCLUSIONS

In summary, surface thermodynamic characteristics of OAN, p-HPA and OAN/p-HPA composites were tested by using 14 IGC methods and molecular models and applied for practical RT CO gas sensing applications. For OAN and the OAN/p-HPA composite, the London dispersive surface free energy values $\gamma_s^d(T)$ decreased as temperature increases. The values of OAN proved to be higher compared with those of the OAN/p-HPA composite because of the higher dispersive surface properties of the OAN surface. In our calculation of the Gutmann Lewis acid−base parameters K_A and K_D the two surfaces showed nearly similar K_A values, whereas the K_D values of the OAN/p-HPA composite were higher than those of OAN. This indicates that the two surfaces contain more basic sites and a smaller number of acidic sites. It is concluded that with the addition of OAN, the number of basic sites on the p-HPA blend surface increases while the number of acidic sites remains constant. Based on our calculation, the OAN/p-HPA composites sensor showed an excellent CO gas sensing performance including high sensitivity and selectivity and good reproductivity. Moreover, the polymeric composite gas sensor showed a significant gas sensing response at different temperatures and RH environments. It is expected that the composite materials are a promising candidate for high-performance RT gas sensing applications based on IGC thermodynamic studies.

■ ASSOCIATED CONTENT

Ⓢ Supporting Information

The Supporting Information is available free of charge at https://pubs.acs.org/doi/10.1021/acsomega.2c03897.

The experimental section, characterization, schematic illustration, deconvoluted XPS core-level spectra, variations of the surface free energy figures of OAN and the OAN/p-HPA composite, variations of ΔG_a^{sp} as a function of temperature for the various polar molecules, and long-term stability test and response/recovery curves are included (PDF)

■ AUTHOR INFORMATION

Corresponding Author

Chang Woo Kim − *Department of Nanotechnology Engineering, College of Engineering, Pukyong National University, Busan 48513, Republic of Korea;* ⓞ orcid.org/ 0000-0001-5821-0041; Email: kimcw@pknu.ac.kr

Authors

Praveen Kumar Basivi − *Pukyong National University Industry-University Cooperation Foundation, Pukyong National University, Busan 48513, Republic of Korea;* ⓞ orcid.org/0000-0002-8214-9532

Tayssir Hamieh − *Faculty of Science and Engineering, Maastricht University, 6200 MD Maastricht, Netherlands; Laboratory of Materials, Catalysis, Environment and Analytical Methods Laboratory (MCEMA), Faculty of Sciences, Lebanese University, 1533 Hadath, Lebanon*

Kedhareswara Sairam Pasupuleti − *Department of Physics, Chungnam National University, Daejeon 34134, Republic of Korea*

Visweswara Rao Pasupuleti − *Center for International Collaboration and Research, REVA University, Bangalore, Karnataka 560064, India;* ⓞ orcid.org/0000-0002-4454-3408

Vempuluru Navakoteswara Rao − *National Nanofab Center, Korea Advanced Institute of Science, Daejeon 34141, Republic of Korea*

Moon-Deock Kim − *Department of Physics and Institute of Quantum Systems (IQS), Chungnam National University, Daejeon 34134, Republic of Korea;* ⓞ orcid.org/0000-0002-7622-8488

Complete contact information is available at:
https://pubs.acs.org/10.1021/acsomega.2c03897

Author Contributions

P.K.B. was involved in conceptualization and writing, T.H. was involved in writing, K.S.P. was involved in validation and writing, V.R.P. was involved in validation, V.N.R. was involved in formal analysis, M-D.K. was involved in review, and C.W.K. supervision, review, and editing.

Notes

The authors declare no competing financial interest.

■ ACKNOWLEDGMENTS

■ REFERENCES

(1) Kumar, B. P.; Rao, P. V.; Hamieh, T.; Kim, C. W. Comparative study of nitrogen doped multi walled carbon nanotubes grafted with carboxy methyl cellulose hybrid composite by inverse gas chromatography and its UV photo detectors application. *J. Chromatogr. A* **2022**, *1670*, 1−15.

(2) Han, X.; Jallo, L.; To, D.; Ghoroi, C.; Davé, R. Passivation of High-Surface-Energy sites of Milled Ibuprofen crystals via dry coating for reduced cohesion and improved flowability. *J. Pharm. Sci.* **2013**, *102*, 2282−2296.

(3) Das, S. C.; Zhou, Q.; Morton, D. A.; Larson, I.; Stewart, P. J. Use of surface distribution by inverse gas chromatography to understand mechano fusion processing and functionality of lactose coated with magnesium state. *Eur. J. Pharm. Sci.* **2011**, *43*, 325−333.

(4) Karde, V.; Ghoroi, C. Influence of surface modification on wettability and surface energy characteristics of pharmaceutical excipient powders. *Int. J. Pharm.* **2014**, *475*, 351−363.

(5) Shah, U. V.; Olusanmi, D.; Narang, A. S.; Hussain, M. A.; Gamble, J. F.; Tobyn, M. J.; Heng, J. Y. Y. Effect of crystal habits on the surface energy and cohesion of crystalline powders. *Int. J. Pharm.* **2014**, *472*, 140−147.

(6) Hao, Q.; Lei, W.; Xie, X.; Xia, M.; Wang, F.; Yang, X. High-quality and excellent green-light-emitting poly (acenaphthylene) film: electro synthesis and characterization. *Polym. Chem.* **2011**, *21*, 085−1090.

(7) McNeill, C. I.; Mohammed, M. H. Thermal degradation behavior of poly(acenaphthylene). *Polym. Degrad. Stab.* **1997**, *55*, 191−198.

(8) Senkevich, J. J. Oxidative chemical vapor deposition of polyacenaphthylene, polyacenaphthene, and polyindane via benzoyl peroxide. *Thin Solid Films* **2014**, *556*, 23−27.

(9) Liu, Z.; Xi, R.; Zhang, Z.; Li, W.; Liu, Y.; Jin, F.; Wang, X. 4-Hydroxyphenylacetic Acid Attenuated Inflammation and Edema via

Suppressing HIF-1α in Seawater Aspiration-Induced Lung Injury in Rats. *Int. J. Mol. Sci.* **2014**, *15*, 12861−12884.

(10) Agbaje, H.; Springer, J. Production and properties of polyacenaphthylene VII. Unperturbed dimensions and chain conformational studies of polyacenaphthylene. *Eur. Polym. J.* **1987**, *23*, 283−286.

(11) Sparnins, V. L.; Chapman, P. J.; Dagley, S. Bacterial Degradation of 4-Hydroxyphenylacetic Acid and Homoprotocatechuic Acid. *J. Bacter.* **1974**, *120*, 159−167.

(12) Praveen Kumar, B.; Ramanaiah, S.; Madhusudana Reddy, T.; Reddy, K. S. Surface Characterization of Cellulose Acetate Propionate by Inverse Gas Chromatography. *Polym. Bull.* **2014**, *71*, 125−132.

(13) Praveen Kumar, B.; Ramanaiah, S.; Madhusudana Reddy, T.; Reddy, K. S. Surface thermodynamics of Efavirenz and a blend of Efavirenz with cellulose acetate propionate by inverse gas chromatography. *Surf. Interface Anal.* **2016**, *48*, 4−9.

(14) Hamieh, T.; Schultz, J. New Approach to Characterize Physicochemical Properties of Solid Substrates by Inverse Gas Chromatography at Infinite Dilution. *J. Chromatogr. A.* **2002**, *969*, 17−25.

(15) Hamieh, T. New methodology to study the dispersive component of the surface energy and acid−base properties of silica particles by inverse gas chromatography at infinite dilution. *Chromsci.* **2022**, *60*, 126−142.

(16) Dorris, G. M.; Gray, D. G. Adsorption of n-alkanes at Zero Surface Coverage on Cellulose Paper and Wood fibers. *J. Colloid Interface Sci.* **1980**, *77*, 353−362.

(17) Hamieh, T. Study of the Temperature Effect on the Surface Area of Model Organic Molecules, the Dispersive Surface Energy and the Surface Properties of Solids by Inverse Gas Chromatography. *J. Chromatogr. A* **2020**, *1627*, 461372.

(18) Hamieh, T.; Rezzaki, M.; Schultz, J. *Colloids Surf., A* **2001**, *189*, 291.

(19) Sawyer, D. T.; Brookman, D. J. Thermodynamically Based Gas Chromatographic Retention Index for Organic Molecules' Using Salt-Modified Aluminas and Porous Silica Beads. *J. Anal. Chem.* **1968**, *40*, 1847−1853.

(20) Saint Flour, C.; Papirer, E. Gas−Solid Chromatography: A Quick Method of Estimating Surface Free Energy Variations Induced by the Treatment of Short Glass Fibers. *J. Colloid Interface Sci.* **1983**, *91*, 69−75.

(21) Donnet, J. B.; Park, S. J.; Balard, H. Evaluation of Specific Interactions of Solid Surfaces by Inverse Gas Chromatography. *Chromatographia* **1991**, *31*, 434−440.

(22) Brendlé, E.; Papirer, E. A New Topological Index T for Molecular Probes Used in Inverse Gas Chromatography for the Surface Nano rugosity Evaluation. *J. Colloid Interface Sci.* **1997**, *194*, 207−216.

(23) Hamieh, T.; Ahmad, A. A.; Roques-Carmes, T.; Toufaily, J. New Approach to Determine the Surface and Interface Thermodynamic Properties of H-β-Zeolite/Rhodium Catalysts by Inverse Gas Chromatography at Infinite Dilution. *Sci. Rep.* **2020**, *10*, 1−27.

(24) Chehimi, M. M.; Abel, M. L.; Perruchot, C.; Delamar, M.; Lascelles, S. F.; Armes, S. P. The determination of the surface energy of conducting polymers by inverse gas chromatography at infinite dilution. *Synth. Met.* **1999**, *104*, 51−59.

(25) Kwon, E. H.; An, H.; Park, M. B.; Kim, M.; Park, Y. D. Conjugated polymer−zeolite hybrids for robust gas sensors: Effect of zeolite surface area on NO$_2$ sensing ability. *Chem. Eng. J.* **2021**, *420*, 129588.

(26) Tsai, Y. S.; Tsai, S. c.; Kuo, C. C.; Chan, W. L.; Lin, W. H.; Wu, Y. C. S.; Lin, Y. S.; Li, M.; Kuo, M. H.; Chen, M. Y. Organic/inorganic hybrid nanostructures of polycrystalline perylene diimide decorated ZnO nanorods highly enhanced dual sensing performance of UV light/CO gas sensors. *Results Phys.* **2021**, *24*, 173.

(27) Pasupuleti, K. S.; Bak, N. H.; Peta, K. R.; Kim, S. G.; Cho, H. D.; Kim, M. D. Enhanced sensitivity of langasite-based surface acoustic wave CO gas sensor using highly porous Ppy@PEDOT: PSS hybrid nanocomposite. *Sens. Actuators, B* **2022**, *363*, 131786.

(28) Mahajan, S.; Jagtap, S. Metal-oxide semiconductors for carbon monoxide (CO) gas sensing: A review. *Appl. Mater. Today* **2020**, *18*, 100483.

(29) Hou, L.; Zhang, C.; Li, L.; Du, C.; Li, X.; Kang, X. F.; Chen, W. CO gas sensors based on p-type CuO nanotubes and CuO nanocubes: Morphology and surface structure effects on the sensing performance. *Talanta* **2018**, *188*, 41−49.

(30) Tropp, J.; Ihde, M. H.; Williams, A. K.; White, N. J.; Eedugurala, N.; Bell, N. C.; Azoulay, J. D.; Bonizzoni, M. A sensor array for the discrimination of polycyclic aromatic hydrocarbons using conjugated polymers and the inner filter effect. *Chem. Sci.* **2019**, *10*, 247.

(31) Walha, F.; Lamnawar, K.; Maazouz, A.; Jaziri, M. Rheological, Morphological and Mechanical Studies of Sustainably Sourced Polymer Blends Based on Poly (Lactic Acid) and Polyamide 11. *Polymer* **2016**, *8*, 61.

(32) Kemball, C.; Rideal, E. K. The adsorption of vapors on mercury (I) Non-polar substances. *Proc. R. Soc. London, Ser. A* **1946**, *187*, 53−73.

(33) Hamieh, T. Determination of the Transition Phenomena of Poly(α-n-alkyl) methacrylates Adsorbed on Silica by Inverse Gas Chromatography. *J Polymer Res.* **2011**, *18*, 1159−1168.

(34) Hamieh, T.; Al-Ali, F.; Ali-Ahmad, A.; Chawraba, K.; Toufaily, J.; Youssef, Z.; Tabaja, N.; Roques-Carmes, T.; Lalevée, J. New Methodology to Determine the Surface Energy, Specific Interactions and Acid−base Properties of Titanium Dioxide by Inverse Gas Chromatography. *Int. J. Chem. Sci.* **2021**, *19*, 1−17.

(35) Kakani, V.; Kim, H.; Basivi, P. K.; Pasupuleti, V. R. Surface Thermo-Dynamic Characterization of Poly (Vinylidene Chloride-Co-Acrylonitrile) (P(VDC-co-AN)) Using Inverse-Gas Chromatography and Investigation of Visual Traits Using Computer Vision Image Processing Algorithms. *Polymer* **2020**, *12*, 1631.

(36) Hamieh, T.; Jrad, A.; Roques-Carmes, T.; Hmadeh, M.; Toufaily, J. Surface thermodynamics and Lewis acid−base properties of metal−organic framework Crystals by Inverse gas chromatography at infinite dilution. *J. Chromatogr. A* **2022**, *1666*, 462849.

(37) Brendlé, E.; Papirer, E.; Balard, H.; Dentzer, J. Variation of the surface properties of nickel o Tide upon heat treatment evidenced by temperature programmed desorption and inverse gas chromatography studies. *J. Mater. Sci.* **2000**, *35*, 3573−3577.

(38) Balard, H.; Sidqi, M.; Papirer, E.; Donnet, J. B.; Tuel, A.; Hommel, H.; Legarnd, A. P. Study of modified silicas by inverse gas chromatography part II: influence of chain length on surface properties of silicas grafted with α−ω diols. *Chromatographia* **1988**, *25*, 712−716.

(39) Kumar, B. P.; Rao, P. V.; Hamieh, T. Surface Thermodynamic Properties of Sodium Carboxymethyl Cellulose by Inverse Gas Chromatography. *Chem. Eng. J. Adv.* **2022**, *9*, 1−10.

(40) Hamieh, T. New Methodology to Study the Dispersive Component of the Surface Energy and Acid−Base Properties of Silica Particles by Inverse Gas Chromatography at Infinite Dilution. *J. Chromatogr. Sci.* **2021**, *60*, 126−142.

(41) Hamieh, T.; Abbasian, A.; Farshchi, N. New Methods to Characterize the Surface and Interface Acid−Base Properties of Some Hydrocarbons by Inverse Gas Chromatography. *Chromatographia* **2020**, *83*, 615−629.

(42) Hamieh, T.; Chawraba, K.; Lalevée, J.; Toufaily, J.New methods for the determination of the surface physicochemical properties and glass transition of polyaniline in conducting and non-conducting forms by using IGC technique at infinite dilution. *J. Mat. Sci & Eng.* **2021**, *10*.

(43) Hamieh, T.On Some Irregularities of the Determination of the Surface Properties of Solid Materials. *J. Mat. Sci & Eng.* **2021**, *10*, 6.

(44) Kumar, B. P.; Sreekanth, T. V. M.; Sivalingam, R.; Thota, C.; Pasupuleti, V. R. Surface characterization and London dispersive surface free energy of functionalized single-walled carbon nanotubes with a blend of polytetrafluoroethylene by inverse gas chromatography. *Surf. Interface Anal.* **2019**, *51*, 516−524.

(45) Gusain, A.; Joshi, N. J.; Vadre, P.; Aswal, D. Flexible NO gas sensor based on conducting polymer poly[*N*-9′-heptadecanyl-2,7-carbazole-alt-5,5-(4′,7′-di-2-thienyl-2′,1′,3′-benzothiadiazole)] (PCDTBT). *Sens. Actuators, B* **2017**, *239*, 734−745.

(46) Ferretti, F.; Rota, L.; Ragaini, F. Unexpected coordination behavior of ruthenium to a polymeric α-diimine containing the poly[*bis*(arylimino)acenaphthene] fragment. *Inorg. Chim. Acta* **2021**, *518*, 120257.

(47) Shin, Y. S.; Chae, B.; Jung, Y. M.; Lee, S. W. Thermal imidization behaviors of 6FDA-ODA poly (amic acid) containing curing accelerators by in-situ FTIR spectroscopy. *Vib. Spectrosc.* **2020**, *106*, 300.

(48) Wang, X. Q.; Gan, W. P.; Xiang, F.; Li, B. Y. Effect of curing agent and curing substrate on low temperature curable silver conductive adhesive. *J. Mater. Sci.: Mater. Electron.* **2019**, *30*, 2829−2836.

(49) Wang, X.; Brigante, M.; Mailhot, G.; Dong, W. Bismuth catalyst mediated degradation of *p*-hydroxyphenylacetic acid: Photoactivation, interfacial mechanism, and influence of some critical parameters. *Chem. Eng. J.* **2018**, *349*, 822−828.

(50) Pasupuleti, K. S.; Reddeppa, M.; Chougule, S. S.; Bak, N. H.; Nam, D. J.; Jung, N.; Cho, H. D.; Kim, S. G.; Kim, M. D. High performance langasite based SAW NO_2 gas sensor using 2D g-C_3N_4@TiO_2 hybrid nanocomposite. *J. Hazard. Mater.* **2022**, *427*, 128174.

(51) Gosh, A.; Zhang, C.; Shi, S.; Zhang, H. High temperature CO_2 sensing and its cross-sensitivity towards H_2 and CO gas using calcium doped ZnO thin film coated langasite SAW sensor. *Sens. Actuators, B* **2019**, *301*, 958.

(52) Dong, J.; Wee, V.; Peh, S. B.; Zhao, D. Molecular-Rotor-Driven Advanced Porous Materials. *Angew. Chem., Int.* **2021**, *60*, 16279−16292.

(53) Hsu, K. C.; Fang, T. H.; Chen, S. H.; Kuo, E. Y. Gas sensitivity and sensing mechanism studies on $ZnO/La_{0.8}Sr_{0.2}Co_{0.5}Ni_{0.5}O_3$ heterojunction structure. *Ceram. Int.* **2019**, *45*, 8744−8749.

(54) Liu, X.; Ling, Y.; Huang, L.; Gao, W. A novel CO sensor based on the point contact between Pd decorated TiO_2 nanotubes array. *J. Nanosci. Nanotechnol.* **2013**, *13*, 869−872.

(55) Steinhauer, S.; Singh, V.; Cassidy, C.; Gspan, C.; Grogger, W.; Sowwan, M.; Köck, A. Single CuO nanowires decorated with size-selected Pd nanoparticles for CO sensing in humid atmosphere. *Nanotechnology* **2015**, *26*, 175502.

(56) Roy, A.; Ray, A.; Sadhukhan, P.; Naskar, K.; Lal, G.; Bhar, R.; Sinha, C.; Das, S. Polyaniline-multiwalled carbon nanotube (PANI-MWCNT): Room temperature resistive carbon monoxide (CO) sensor. *Synth. Met.* **2018**, *245*, 182−189.

(57) Zhuiykov, S. Carbon monoxide detection at low temperatures by semiconductor sensor with nanostructured Au-doped CoOOH films. *Sens. Actuators, B* **2008**, *129*, 431−441.

(58) Paul, S.; Amalraj, F.; Radhakrishnan, S. CO sensor based on polypyrrole functionalized with iron porphyrin. *Synth. Met.* **2009**, *159*, 1019−1023.

(59) Sayed, S.; Abd El-Moneim, A. M.; Fath El Bab, A. R.; Ahmed, M. R.; Nakamura, K. High-Performance Carbon Monoxide Gas Sensor based on Graphene. *Int. J. Eng. Res. Technol.* **2015**, *4*, 518−523.

(60) Densakulprasert, N.; Wannatong, L.; Chotpattananont, D.; Hiamtup, P.; Sirivat, A.; Schwank, J. Electrical conductivity of polyaniline/zeolite composites and synergetic interaction with CO. *Mater. Sci. Eng., B* **2005**, *117*, 276−282.

■ NOTE ADDED AFTER ASAP PUBLICATION

After this paper was published ASAP October 7, 2022, errors were corrected in the TOC/abstract graphic and in Figure S1 in the Supporting Information. The corrected version was reposted October 18, 2022.